

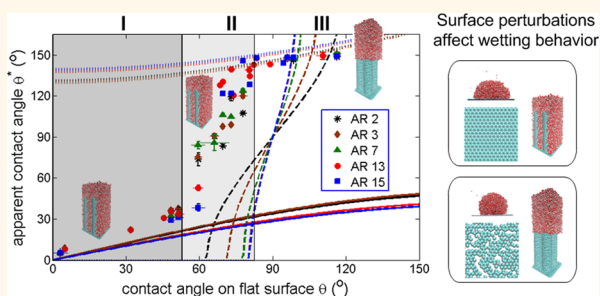
# Capturing Wetting States in Nanopatterned Silicon

XiuMei Xu,<sup>†,\*</sup> Guy Vereecke,<sup>†</sup> Chang Chen,<sup>†,‡</sup> Geoffrey Pourtois,<sup>†,§</sup> Silvia Armini,<sup>†</sup> Niels Verellen,<sup>†,‡</sup> Wei-Kang Tsai,<sup>⊥</sup> Dong-Wook Kim,<sup>||</sup> Eunsongyi Lee,<sup>||</sup> Chang-You Lin,<sup>‡</sup> Pol Van Dorpe,<sup>†,‡</sup> Herbert Struyf,<sup>†</sup> Frank Holsteyns,<sup>†</sup> Victor Moshchalkov,<sup>‡</sup> Joseph Indekeu,<sup>‡</sup> and Stefan De Gendt<sup>†,‡</sup>

<sup>†</sup>IMEC, Kapeldreef 75, Leuven 3001, Belgium, <sup>‡</sup>Department of Physics and Astronomy, Department of Chemistry, KU Leuven, Leuven 3001, Belgium, <sup>§</sup>Department of Chemistry, PLASMANT, University of Antwerp, B-2610 Wilrijk, Belgium, <sup>⊥</sup>Department of Material Science and Engineering, University of Southern California, Los Angeles, California 90089, United States, and <sup>||</sup>Department of Physics, Ewha Womans University, Seoul 120-750, Korea

**ABSTRACT** Spectacular progress in developing advanced Si circuits with reduced size, along the track of Moore's law, has been relying on necessary developments in wet cleaning of nanopatterned Si wafers to provide contaminant free surfaces. The most efficient cleaning is achieved when complete wetting can be realized. In this work, ordered arrays of silicon nanopillars on a hitherto unexplored small scale have been used to study the wetting behavior on nanomodulated surfaces in a substantial range of surface treatments and geometrical parameters. With the use of optical reflectance measurements, the nanoscale water imbibition depths have been measured

and the transition to the superhydrophobic Cassie–Baxter state has been accurately determined. For pillars of high aspect ratio (about 15), the transition occurs even when the surface is grafted with a hydrophilic functional group. We have found a striking consistent deviation between the contact angle measurements and the straightforward application of the classical wetting models. Molecular dynamics simulations show that these deviations can be attributed to the long overlooked atomic-scale surface perturbations that are introduced during the nanofabrication process. When the transition condition is approached, transient states of partial imbibition that characterize intermediate states between the Wenzel and Cassie–Baxter states are revealed in our experiments.



**KEYWORDS:** nanoscale wetting · transient states · Cassie–Baxter · Wenzel · hemiwicking · optical reflectance spectroscopy · molecular dynamics simulations

The wettability of a surface is often characterized by water contact angles. On an ideal smooth surface, the static water contact angle depends on the interfacial energy balance and is well described by Young's equation.<sup>1–6</sup> On the other hand, on a rough substrate, the wetting behavior can be quite different and varies from superhydrophilic to superhydrophobic.<sup>2,3,5,7–11</sup> Among numerous applications of different wetting regimes, reliable wet cleaning of nanopatterned Si wafers is an extremely important issue in modern technology. In the end, it is one of the essential factors defining the limits of the powerful modern Si technology as it has been advancing and scaling along Moore's law. The realization of the hydrophilic regime plays a crucial role here and potential incomplete wetting of the nanopatterned Si surfaces could impede the applicability of the Si technology due to

the absence of reliable wet cleaning at the nanoscale.

The influence of topography and artificial surface modulation on wetting is normally studied by plotting the apparent contact angle on a rough substrate ( $\theta^*$ ) as a function of the contact angle on a flat surface ( $\theta$ ). Three distinct wetting states have been observed:<sup>7,12</sup> (i) the superhydrophilic hemiwicking state in which water spontaneously penetrates the grooves and travels beyond the apparent drop;<sup>5,13,14</sup> (ii) Wenzel's model describing another complete wetting state in which water fills the surface landscape underneath the drop;<sup>3,13–15</sup> (iii) the superhydrophobic Cassie–Baxter state, sometimes referred to as the lotus effect, and often characterized by a large apparent contact angle and small hysteresis due to air trapping underneath the drop.<sup>3,5,9,11,12,15</sup> Superhydrophobic properties are desired for applications such as self-cleaning or

\* Address correspondence to xiumei@imec.be.

Received for review October 28, 2013 and accepted December 31, 2013.

Published online December 31, 2013  
10.1021/nn405621w

© 2013 American Chemical Society

drag reduction.<sup>16,17</sup> In contrast, for applications that require good wetting, mixing, or transport in between the structures, such as wafer cleaning in micro- and nanoelectronics fabrication processes,<sup>18</sup> superhydrophobicity should be avoided.<sup>19,20</sup> Therefore, it is of utmost importance to identify the transition criteria between different wetting states. In thermodynamic equilibrium, the stable wetting state corresponds to the one with the minimum surface free energy. A simple calculation allows one to derive the transition thresholds between different wetting states as a function of the geometrical factors.<sup>3,5,8,14,21</sup> Equations 1–5 give the transition criteria for different wetting models.

#### Hemiwicking:

$$\cos\theta^*_h = f_s \cos\theta + 1 - f_s, \quad (0 < \theta < \theta_c^{(1)}) \quad (1)$$

#### Wenzel:

$$\cos\theta^*_W = r \cos\theta, \quad (\theta_c^{(1)} < \theta < \theta_c^{(2)}) \quad (2)$$

#### Cassie–Baxter:

$$\cos\theta^*_{C-B} = f_s \cos\theta - 1 + f_s, \quad (\theta > \theta_c^{(2)}) \quad (3)$$

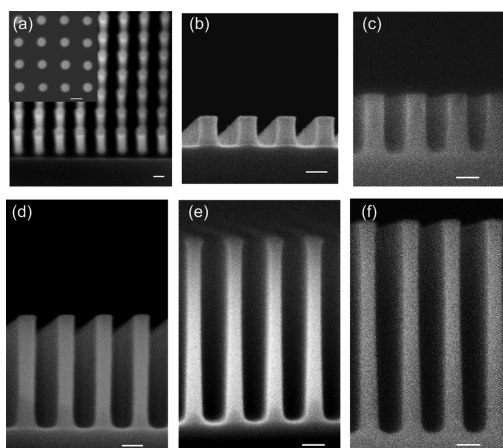
where,

$$\theta_c^{(1)} = \cos^{-1}((1 - f_s)/(r - f_s)) \quad (4)$$

$$\theta_c^{(2)} = \cos^{-1}((f_s - 1)/(r - f_s)) \quad (5)$$

For hemiwicking and Cassie–Baxter states, the apparent drop lies on top of a composite interface and the relevant geometrical factor is the top solid surface fraction,  $f_s$ . For the Wenzel model, the apparent contact angle depends on the ratio of the total surface area to the projected area,  $r$ .

An analysis of contact angle measurements in terms of the classic wetting models requires the geometrical factors in eqs 1–5 to be given *a priori*, which is quite challenging for many natural<sup>22–24</sup> or artificially synthesized surfaces with nonperiodic patterns.<sup>7,25,26</sup> The development of microfabrication processes allows one to obtain artificial ordered arrays of structures with well-defined geometries.<sup>15,21,27,28</sup> The reported contact angles are often observed to be higher than those predicted by the Wenzel model, and sometimes a Cassie–Baxter state is observed when the classic models give a stable Wenzel state.<sup>26–28</sup> The postulated reasons for these discrepancies are inaccurate estimations of geometrical factors,<sup>25,26</sup> contact line pinning,<sup>26,29</sup> air trapping facilitated by the nonuniform structure profiles,<sup>30–32</sup> or hierarchical surface topography.<sup>24,33</sup> In a metastable Cassie–Baxter state, there is an energy barrier in the weakly hydrophobic regime, and the transition to the Wenzel state can be triggered spontaneously by capillary pressure<sup>34–36</sup> or by external pressure.<sup>34</sup> The investigation of the wetting transition is a very active research area, crucial, among other things, for modern nanotechnology. In this work, we use silicon nanopillars with well-defined profiles to



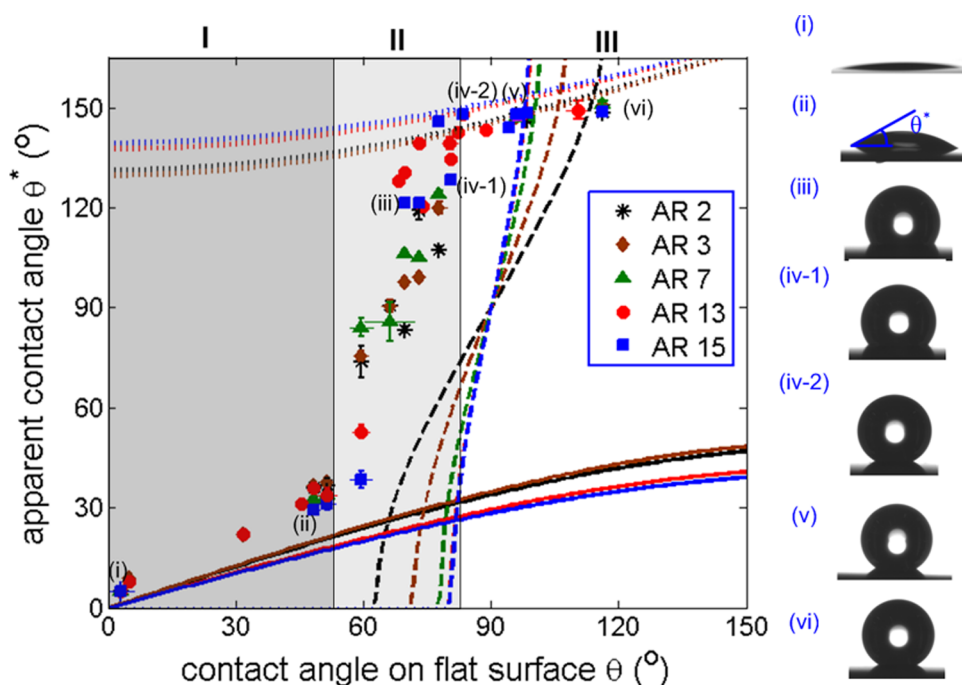
**Figure 1.** SEM images of the silicon nanopillars. (a) Tilted view of the square packed pillar arrays; a top view is shown in the inset. (b–f) Cross-sectional SEM images of nanopillars of aspect ratio (AR) 2, 3, 7, 13 and 15, respectively. The scale bars are 50 nm.

study the wetting behavior influenced by nanopatterning, and the wetting state is determined accurately by using novel optical-based reflectance measurements. Molecular dynamics simulations are carried out to investigate the wetting mechanism.

## RESULTS AND DISCUSSION

**Structures.** An ordered array of nanopillars is etched into a 300 mm silicon wafer.<sup>37</sup> The pillar arrays are square packed with a 90 nm pitch ( $p$ ) and the pillars have diameters ( $d$ , 33–43 nm) and heights ( $h$ , 70–460 nm) (Figure 1). The uniform profiles allow us to determine accurately the geometrical factors in eqs 1–5 (*cf.* Supporting Information).

**Surface Treatments.** To modify the intrinsic wettability of the nanopillars, different treatments are used to functionalize the silicon surface. All aqueous-based treatments are ruled out because the high surface tension of water can cause pattern collapse of the nanopillars. Most of the surface functionalization is performed in the vapor or gas phase, including UV O<sub>3</sub> cleaning, vapor HF etching, vapor phase deposition of decamethyl tetrasiloxane, dodecamethyl pentasiloxane and self-assembled monolayers of CUTS (11-cyanoundecyltrichlorosilane), PETS (phenethyltrichlorosilane), BUTS (11-bromoundecyltrichlorosilane) and FDTS (1*H*,1*H*,2*H*,2*H*-perfluoro-decyltrichlorosilane). To have a well distributed coverage of the range of water contact angles, monolayers of PEO (methoxy(polyethyleneoxy)propyltrimethoxysilane), MPTMS (3-mercaptopropyltrimethoxysilane) and APTMS (3-aminopropyltrimethoxysilane) are also grafted on nanopillars in anhydrous toluene. To minimize the influence of surface contamination, all samples are prepared freshly and the surface treatments and measurements are performed in a class 1 cleanroom environment at 35% humidity and 22 °C. Details of



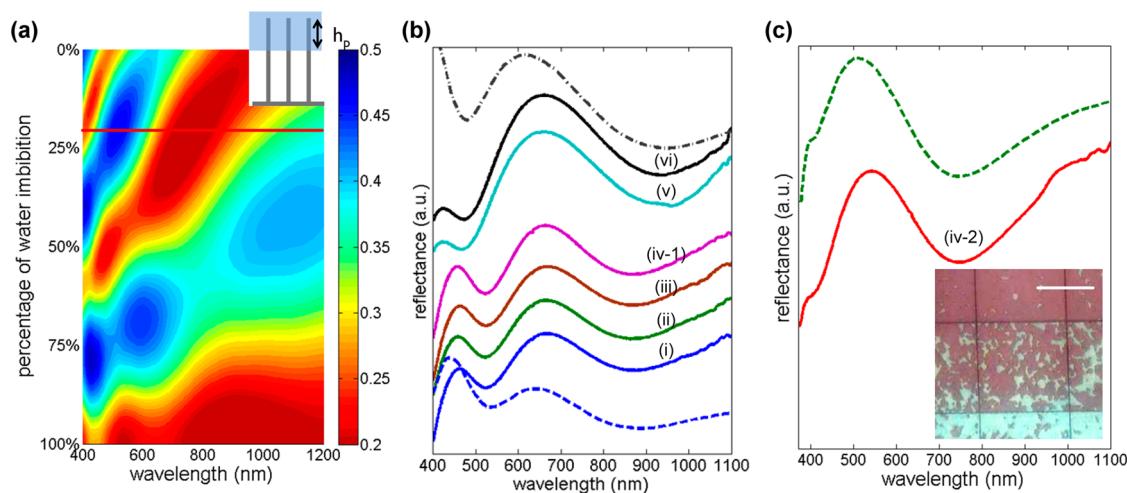
**Figure 2.** The apparent contact angle ( $\theta^*$ ) on nanopillars as a function of the contact angle ( $\theta$ ) measured on a flat silicon wafer. Symbols are measurements for pillars with different aspect ratios (AR) and curves are theoretical predictions for hemiwicking (solid lines), Wenzel (dashed lines) and Cassie–Baxter models (dotted lines). Note the theoretical curves calculated for each AR are plotted with the same color as the corresponding symbols and some curves overlap due to the closeness in the geometrical factors. Pictures on the right (i–vi) give the side view photographic images of sessile drops ( $\Phi \sim 1.5$  mm) on pillars of AR 15, corresponding to the marked measurement points (blue squares) in the plot.

the surface treatments are given in Supporting Information.

**Contact Angle Measurements.** The topographic influence on wetting is shown in Figure 2, where the apparent water contact angles on the nanopillars ( $\theta^*$ ) are plotted against the contact angles on flat silicon wafers with the same surface functionalization ( $\theta$ ). The theoretical curves of the hemiwicking (solid curves), Wenzel (dashed curves) and Cassie–Baxter (dotted curves) states are plotted using the geometrical factors listed in Table S1 in Supporting Information. Our data show three wetting regimes. I: for contact angles ( $\theta$ ) less than  $55^\circ$ , the data follow the trend of hemiwicking wetting. Since the top solid surface fractions are similar for all arrays, the apparent contact angles are alike for pillars of different heights. II: for  $55^\circ < \theta < 80^\circ$ , there is a sharp increase in the apparent contact angles. Wenzel's model predicts that the increase in the total surface area should enhance wetting. However, the apparent contact angles we measured are consistently much higher than those on flat surfaces. In this regime, the pillar height strongly affects the contact angle data, but there is a trend break in its effect on wetting. For  $55^\circ < \theta < 65^\circ$ , wetting is enhanced by an increase in the surface area and for taller pillars the apparent contact angles are lower, while for  $65^\circ < \theta < 80^\circ$ , the wettability diminishes with increasing pillar height. III: for  $\theta > 80^\circ$ , the apparent contact angles exceed  $140^\circ$ , and there is good agreement with the Cassie–Baxter model.

Remarkably, the dependence of  $\theta^*$  on  $\theta$  in Figure 2 is insensitive to the surface treatments that have been used. When comparing the self-assembled monolayer deposition of CUTS with vapor HF etch treatment, we find that both of them give very similar results on planar silicon wafers as well as on nanopillars despite the very different surface functionalization mechanism. Therefore, we can rule out the influence of chain length and orientation of the self-assembled monolayer molecules on the contact angle measurements.

In our experiments, the pillars have uniform profiles and there is no apparent surface roughness in SEM images with subnanometer pixel resolutions. In order to determine whether the deviations observed in the contact angles are due to air trapping underneath the water drops, some quantitative inspection techniques are needed. In the literature, measurements of contact angle hysteresis are the most commonly used methods to distinguish Cassie–Baxter from Wenzel states of wetting.<sup>38–41</sup> However, there is no agreed-upon model for the contact angle hysteresis, and the reported hysteresis can vary quite a lot depending on the surface topography and treatments.<sup>24,39–41</sup> Interference microscopy has been used to measure the liquid penetration and the meniscus profiles underneath the drop,<sup>42</sup> but this technique is applicable only when the substrate is made of transparent material and the patterned structures are on the micrometer scale. Acoustic reflection techniques enable quantitative



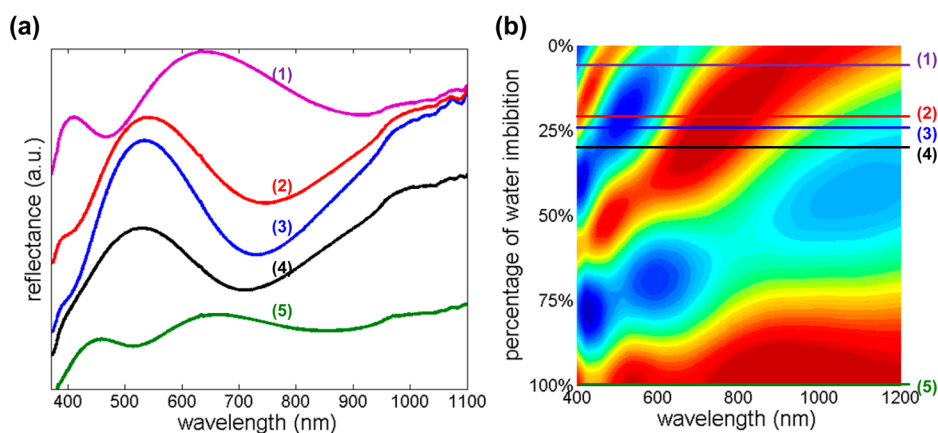
**Figure 3.** (a) FDTD simulations showing a contour map of the reflectance as a function of wavelength and the percentage of water imbibition depth, in which red denotes low reflectance and dark blue high reflectance as indicated in the color bar. A homogeneous instantaneous water penetration depth ( $h_p$ ) is assumed in the simulation as shown in the inset. (b) Stacked reflection spectra measured on aspect ratio 15 pillars with different surface treatments (solid lines i–vi). The corresponding side view images of water drops on such surfaces are given in Figure 2i–vi. The simulated spectra at 100% (dashed curve) and 2% (dash-dotted curve) water imbibition are also plotted for reference. (c) Near the transition (the contact angle  $\theta$  is about  $82^\circ$  in Figure 2), partial water penetration has been measured (solid line iv-2), and the dashed curve is a simulation of 22% water penetration (thin line in (a)). The inset is a microscope image showing the coexistence of different wetting states, in which the bright area corresponds to the Cassie–Baxter state and the dark area denotes where partial water imbibition takes place. The scale bar is 50  $\mu\text{m}$ . The array consists of  $80 \times 80 \mu\text{m}^2$  subarrays of nanopillars.

wetting depth measurement for micrometer size pillars.<sup>43</sup> To the best of our knowledge, there are no inspection techniques that could be used for quantitative wetting depth measurements in nanostructures.

**Optical Reflectance Measurements.** Nanostructures often exhibit unique optical properties due to the inherent light confinement, *e.g.*, silicon nanopillars of different dimensions can display a variety of colors in air due to the variations in the guided light modes.<sup>44</sup> Since the diameter and the pitch of the pillars used in this study are very small, the resonant guided mode appears in the short wavelength range ( $<400$  nm). Thus, multiple beam interference between the top and bottom interfaces of the pillar array dominates the reflectance spectra in the visible range. When the air surrounding the nanopillars is partially or completely replaced by the water, the difference in refractive index can result in a big change in the optical reflectance spectra. Figure 3a shows the finite difference time domain (FDTD) simulation results of the reflectance response when the instantaneous water imbibition depth is assumed to be homogeneous and it increases from 0% (Cassie–Baxter state) to 100% (hemiwicking or Wenzel state). In the simulations, the nanopillars are modeled as cylinders with dimensions corresponding to AR 15. There are some resonant modes present due to the constructive interference of beams reflected at different interfaces (*cf.* Supporting Information). The resonant wavelengths are very sensitive to any change in refractive index, and thus can be used to determine the water imbibition depths.

Figure 3b shows the measured reflection spectra for nanopillars of AR15 in different wetting regimes. Pillars with UV  $\text{O}_3$  cleaning have the most hydrophilic surface termination (Figure 2i), and thus are used as the reference for complete water penetration. There are two resonant dips in the reflectance spectra corresponding to the first and the second order modes. Compared with the FDTD simulations of complete wetting (dashed curve), there is a slight mismatch (about 10 nm) in the resonant wavelengths, which might be due to the curvature at the bottom of the pillars as can be seen from the SEM images (Figure 1). For pillars with MPTMS (Figure 2ii), CUTS (Figure 2iii) coatings, despite the very different apparent contact angles, the measured spectra are identical to the ones obtained with UV  $\text{O}_3$  treated pillars. This indicates that in wetting regime II, there is a Wenzel state although the measured contact angles are much higher than the Wenzel predictions. In wetting regime III, both BUTS (Figure 2v) and FDTS (Figure 2vi) deposited pillars give apparent contact angles above  $145^\circ$ . In the reflectance spectra, as compared to the ones for pillars with hydrophilic functional groups, a red-shift (or blue-shift) is observed for the first (or the second) order interference mode. There is excellent agreement with the simulated spectrum of 2% water imbibition (dash-dotted curve), and therefore a Cassie–Baxter state is indeed reached in wetting regime III.

With this knowledge of the actual wetting states, it can be seen from Figure 2 that the measured Wenzel curves are shifted toward the hydrophilic regime. From the extrapolations of the contact angle measurements,



**Figure 4.** Partial and transient water penetration on PETS coated pillars (AR 15, Figure 2(iv-2)). (a) Stacked reflection spectra measured at different locations after the sample is immersed in water. (b) Lines on FDTD simulations mark the corresponding wetting depths for spectra in (a).

the Wenzel to Cassie–Baxter transition happens when the contact angle  $\theta$  is around  $80^\circ$  for AR 15 pillars. Near the transition, the free energies for Wenzel and Cassie–Baxter states are close to each other and interesting dynamic features could arise. By varying the deposition conditions, the contact angles on a PETS coated flat silicon wafer can be fine-tuned in the range of  $77$ – $82^\circ$ , which is close to the transition. The measured apparent contact angles on AR 15 pillars range from  $128^\circ$  (Figure 2iv-1) to  $146^\circ$  (Figure 2iv-2). When the apparent contact angles are low (Figure 2 iv-1), the optical reflectance spectrum shows a Wenzel state of wetting (as shown in Figure 3b). For PETS with  $\theta$  around  $82^\circ$  (Figure 2iv-2), although the apparent contact angles are similar to those in the Cassie–Baxter states, we observe a gradual breakdown of the superhydrophobic state after immersing the sample in water, and the water imbibition process can take tens of minutes. The inset of Figure 3c is a top view microscope image showing the coexistence of different wetting states on a larger length scale. The bright area in the image corresponds to the place where the Cassie–Baxter state is long-lived (as confirmed by the reflectance spectrum measurements), while in the dark area water imbibition is taking place. Different degrees of water penetration have been measured during the experiments, from complete wetting as in the Wenzel state to partial penetration. Figure 3c shows one of the partial penetration spectra measured with PETS deposited pillars, in which only one resonant dip is observed. There is excellent agreement with the simulated spectrum for 22% water penetration.

This partial water penetration is transient and evolves to complete wetting in a time span of tens of minutes. Figure 4a shows the reflectance spectra measured at different locations after the PETS coated pillars (AR 15) are immersed in water. All the spectra are collected at locations where the color is uniform. Thus, good agreements with FDTD simulations, which assume homogeneous wetting depths, can be obtained.

The lines in the FDTD simulations in Figure 4b mark the corresponding wetting depths for different spectra in Figure 4a.

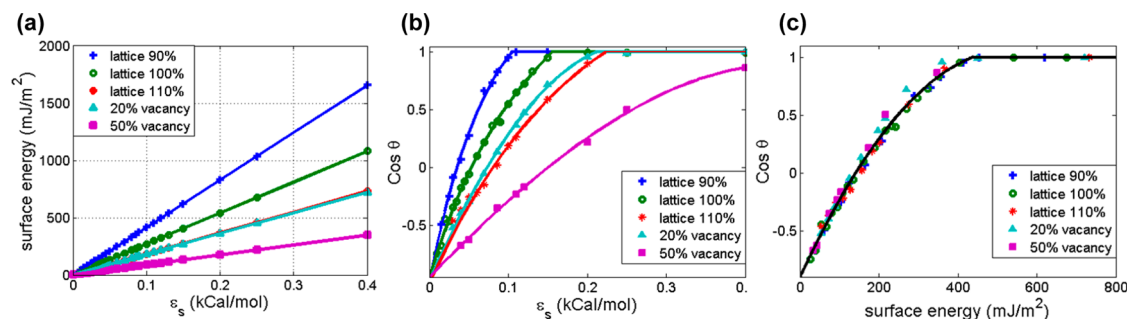
For pillars with lower aspect ratios (AR 2–7), the transition to the superhydrophobic Cassie–Baxter states occurs at larger contact angles ( $\theta$ ), as the critical angle in the transition criterion eq 5 increases with a decrease in surface area ( $r$ ). For pillars of all aspect ratios, the measured transition criteria are consistently lower than the theoretical criteria in eq 5, as can be seen from the shift of the measurements in the Wenzel states (wetting regime II) in Figure 2.

**Molecular Dynamics (MD) Simulations.** The optical reflectance measurements show that the transition to the Cassie–Baxter state actually happens before the theoretical criterion eq 5 is met, and for AR 15 pillars it is even found to take place in the hydrophilic regime. Many publications report a metastable Cassie–Baxter state before the transition criterion is met, which is thought to be related to the energy barrier in the weakly hydrophobic regime.<sup>21,34,45</sup> However, for structures like ours, without reentrant profiles, there is no energy barrier in the hydrophilic regime that prevents water from penetrating and wetting most of the sidewall surfaces.<sup>21,31,40</sup> In order to reveal the underlying mechanism for the discrepancy between the theoretical models and the experiments, 3D molecular dynamics simulations have been carried out using the LAMMPS package.<sup>46</sup>

A hexagonally packed lattice is employed to build both planar and pillared surfaces.<sup>47,48</sup> A hexagonal honeycomb lattice is specifically chosen in order to avoid building cylindrical pillars with many facets, as corners will result in more contact angle hysteresis. The atoms on the substrates are fixed and separated by  $1.42 \text{ \AA}$ , and the distance between adjacent layers is  $3.4 \text{ \AA}$ . By tuning the amplitude of the Lennard-Jones (LJ) potentials for the atoms in the solid ( $\epsilon_s$ ), the interaction energy with water is modified and substrates with different wettability can be simulated (*cf.* Supporting

**TABLE 1. Summary of the Equilibrium Wetting States Calculated with MD Simulations for Pillars of Different Size and Wettability**

$d$ (Å)	$h$ (Å)	$p$ (Å)	$\theta_c$	$\theta = 34^\circ$	$\theta = 66^\circ$	$\theta = 93^\circ$	$\theta = 100^\circ$	$\theta = 110^\circ$	$\theta = 118^\circ$
20	90	30	$96^\circ$	Wenzel	Wenzel	Wenzel	C–B	C–B	C–B
10	100	30	$102^\circ$	Wenzel	Wenzel	Wenzel	Wenzel	C–B	C–B



**Figure 5.** For planar substrates with different surface modifications, the surface energy (a) and contact angles (b) can be quite different even for the same atomic interaction energy  $\epsilon_s$ . (c) The contact angles fall onto a single curve when plotted versus the calculated surface energy.

Information). Contact angles on a smooth surface are determined by fitting the periphery of an equilibrium water drop in the density field.<sup>49</sup> Cylindrical pillars with different dimensions are packed in a square array, and the pitch  $p$  is fixed to 30 Å. To avoid any influence from the large capillary pressure of a tiny droplet ( $\Phi \sim 6$  nm) on the wetting behavior, a layer of equilibrated water molecules is initially placed on top of the pillars and periodic boundary conditions are applied to account for a uniform array. Table 1 compares the equilibrated wetting states after 10 ns obtained for pillars with different diameters ( $d$ ), heights ( $h$ ) and wettability ( $\theta$ ). The theoretical transition criterion angle  $\theta_c$ , obtained using eq 5, is found to be in good agreement with the simulation.





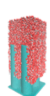

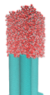








The MD simulations reproduce the predictions of classical models and show that the wetting transitions are properly described by eq 5. In the experiments, there is, however, a consistent shift in the contact angles, implying an early transition to the Cassie–Baxter state. In the MD results given in Table 1, the pillar surface has the same atomic arrangement as the planar substrate; thus, the interaction energy with water is the same for both surfaces. On the other hand, during the fabrication, there are inevitable modifications of the pillar surface with respect to the planar silicon wafer. One possible source of surface alterations arises from the difference in crystal plane orientations, which can result in very different contact angles.<sup>50</sup> Compared with the (100) plane on a planar silicon wafer, the surface of the studied nanopillars consists of mixed crystal planes such as (110), (111) *etc.*, which are well-known to have different atomic densities and surface energies. Another possible surface modification of the pillars could reside in atomic-scale lattice defects induced by the fabrication process. Commercially

available Si planar wafers are polished and the surfaces are characterized by atomically smooth terraces, on the other hand there are more surface defects on nanostructures due to random ion bombardments or atomic scale inhomogeneous chemical etching. To account for these effects in MD simulations, we implement two types of surface alterations. One relates to the change in surface density of an atomically smooth surface and is realized by increasing (or decreasing) the in-plane lattice constant by 10%. The other surface alteration is introduced by randomly creating 20% (or 50%) of atomic vacancies in the top layer.

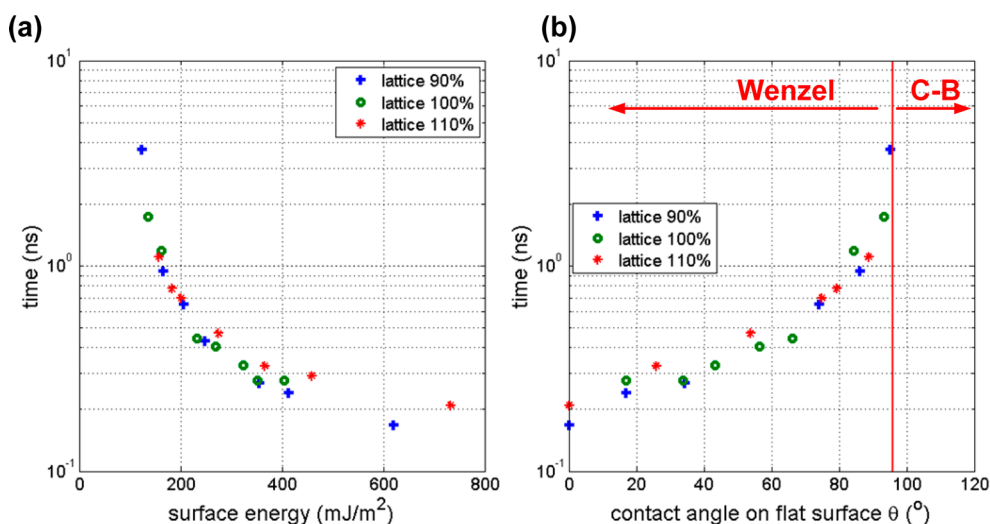
The impact of these surface modifications on wetting is first studied on planar surfaces. To quantify their influence, we calculate the surface energy defined as the excess free energy per unit area of creating a surface from bulk material.<sup>51</sup> Figure 5 shows the surface energy (a) and contact angles (b) calculated on planar substrates as a function of the LJ well depth  $\epsilon_s$ . By increasing  $\epsilon_s$ , the surface energy of the substrate as well as the water–substrate intermolecular interaction energy ( $\epsilon_{ij}$ , *cf.* Supporting Information) are augmented, which results in a lower contact angle and better wettability. For different atomic arrangements, due to the variation in the effective surface density, the surface energies are different. Increasing the lattice constant or the number of atomic vacancies lowers the effective surface density. As a result, the surface energy and wettability are reduced as reflected by the increase in contact angle. When the contact angles are plotted as a function of the surface energy, the results for different surface modifications fall on a universal curve as shown in Figure 5c.

The aforementioned surface modifications also affect wetting on pillars. In the MD simulations shown in

**TABLE 2. MD Simulations of Wetting on Pillars ( $d = 20 \text{ \AA}$ ,  $h = 90 \text{ \AA}$ ,  $p = 30 \text{ \AA}$ ) at Different Time Intervals<sup>a</sup>**

Surface density ( $\text{\AA}^{-2}$ )	Top layer vacancy fraction	Surface energy ( $\text{mJ/m}^2$ )	Contact angle on modified flat surface ( $\theta$ )	Wetting on pillars $d=20 \text{ \AA}$ , $h=90 \text{ \AA}$ , $p=30 \text{ \AA}$		
				0.4 ns	1.5 ns	4 ns
0.47	0%	206.9	74.1°			
0.38	0%	135.1	93.3°			
0.32	0%	91.6	105.0°			
0.38	20%	90.2	107.0°			
0.38	50%	43.5	128.7°			

<sup>a</sup> The LJ potential well depth,  $\epsilon_s = 0.05 \text{ kcal/mol}$ . The surface lattice density, atomic vacancy fractions in the top layer, surface energy and contact angles on the modified flat surfaces are compared.



**Figure 6.** In the MD simulations, for pillars ( $d, 20 \text{ \AA}$ ;  $h, 90 \text{ \AA}$ ;  $p, 30 \text{ \AA}$ ) with different lattice constant scaling, the time needed for complete wetting is plotted against (a) the surface energies of the pillar surface in planar form, and (b) the contact angles measured on a flat surface with the same lattice constant as the pillar surface. The theoretical transition criterion calculated using eq 5 is shown as the vertical solid line in (b).

Table 2, the Lennard-Jones potentials of the atoms in the solid are kept constant and the atomic arrangements are varied on the pillar surface. The surface packing densities, atomic vacancies in the top layer, surface energies and contact angles on the flat surface with the same modifications are compared. Although

the implemented surface modifications are all at the atomic scale, the impact on surface wettability is quite significant as can be seen from the sessile drop profiles and contact angles in Table 2. Snapshots showing the evolution of the water molecule positions on the pillars are taken at fixed time intervals. In Figure 6, the

complete wetting time is plotted as a function of (a) surface energy and (b) contact angle on a flat surface with the same atomic characteristics as the pillar surface ( $\theta$ ). The vertical solid line in Figure 6(b) marks the transition between the Wenzel and Cassie–Baxter states calculated with eq 5. When the surface energy and wettability of the pillar surface are reduced, the wetting speed is lower due to a weaker driving force. The wetting time increases exponentially rapidly when the transition is approached. This is in line with our experiments, in which a slow water imbibition is observed near the transition and a transient intermediate state in between the Wenzel and Cassie–Baxter states is captured by the optical reflectance measurements.

In the experiments (Figure 2), planar silicon wafers are used to characterize the contact angles on the modified surface. However, as compared to planar silicon wafers, additional modifications could be introduced to the pillar surface during the nanofabrication process. These also affect the packing density of the surface functional groups in the following surface treatment steps. As a result, a shift in the measured contact angles is observed in Figure 2.

## CONCLUSIONS

For investigations of wetting at the nanoscale, one of the main drawbacks is the lack of a reliable metrology to evaluate the actual wetting state in nanostructures. In this work, novel optical-based reflectance measurements are utilized to determine quantitatively instantaneous water imbibition depths and to define the actual wetting state on nanopillars. The wetting of nanopillars with different dimensions and surface functionalization is studied systematically. Three regimes are encountered, corresponding to the hemiwicking, Wenzel and Cassie–Baxter states.

A systematic deviation between the theoretical predictions and the measurements is observed. In some cases, the transition to the superhydrophobic Cassie–Baxter state is found to happen even in the hydrophilic regime. Molecular dynamics simulations suggest the deviation could be due to atomic scale surface modifications of the pillar surface. In the nanofabrication process, these are inevitable and include, among others, different crystal plane orientations or atomic-scale surface defects. Compared to a planar wafer surface, the modified pillar surface in planar form can have very different surface energy and wettability. The fabrication-induced surface modifications also affect the packing density of the surface functional groups in a consistent way. As a result, the dependence of  $\theta^*$  on  $\theta$  is universal with respect to the surface treatments used. Near the transition between the Wenzel and Cassie–Baxter states, the wetting speed is significantly reduced, and transient intermediate states with partial water imbibition in nanostructures

can, remarkably, be captured by optical reflectance measurements.

Our results provide an incentive to revisit some of the early works in the light of the impact of surface modifications on wetting properties of micro- and nanomachined structures, as similar surface topography modifications can be introduced by etching (applicable for crystal structures and metals) or can be transferred from the template molds (applicable for soft materials). Awareness of such potential influence is particularly important for the study of the metastable Cassie–Baxter state and the forced transition to the Wenzel state.

**Conflict of Interest:** The authors declare no competing financial interest.

**Acknowledgment.** The paper is dedicated to Professor G. M. (Bud) Homay for the event of his 70th birthday. The authors would like to give their thanks to Professor G. M. (Bud) Homay and Professor P. H. Steen for their constructive comments on the paper. C.C. and N.V. acknowledge financial support from the F.W.O. (Flanders). N.V. and V.V.M. are supported by the Methusalem funding by the Flemish Government.

**Supporting Information Available:** Details of structure dimensions, contact angle measurements, optical reflectance measurements, FDTD simulations and molecular dynamics simulations are given. This material is available free of charge via the Internet at <http://pubs.acs.org>.

## REFERENCES AND NOTES

- De Gennes, P. G. Wetting: Statics and Dynamics. *Rev. Mod. Phys.* **1985**, *57*, 827–863.
- Quééré, D. Non-Sticking Drops. *Rep. Prog. Phys.* **2005**, *68*, 2495–2532.
- Feng, X.; Jiang, L. Design and Creation of Superwetting/Antiwetting Surfaces. *Adv. Mater.* **2006**, *18*, 3063–3078.
- Verplanck, N.; Coffinier, Y.; Thomy, V.; Boukherroub, R. Wettability Switching Techniques on Superhydrophobic Surfaces. *Nanoscale Res. Lett.* **2007**, *2*, 577–596.
- Quééré, D. Wetting and Roughness. *Annu. Rev. Mater. Res.* **2008**, *38*, 71–99.
- Bonn, D.; Eggers, J.; Indekeu, J.; Meunier, J.; Rolley, E. Wetting and Spreading. *Rev. Mod. Phys.* **2009**, *81*, 739–805.
- Onda, T.; Shibuichi, S.; Satoh, N.; Tsujii, K. Super-Water-Repellent Fractal Surfaces. *Langmuir* **1996**, *12*, 2125–2127.
- Bico, J.; Thiele, U.; Quééré, D. Wetting of Textured Surfaces. *Colloids Surf., A* **2002**, *206*, 41–46.
- Erbil, H. Y.; Demirel, A. L.; Avci, Y.; Mert, O. Transformation of a Simple Plastic into a Superhydrophobic Surface. *Science* **2003**, *299*, 1377–1380.
- Feng, X. J.; Feng, L.; Jin, M. H.; Zhai, J.; Jiang, L.; Zhu, D. B. Reversible Super-Hydrophobicity to Super-Hydrophilicity Transition of Aligned ZnO Nanorod Films. *J. Am. Chem. Soc.* **2004**, *126*, 62–63.
- Furstner, R.; Barthlott, W.; Neinhuis, C.; Walzel, P. Wetting and Self-Cleaning Properties of Artificial Superhydrophobic Surfaces. *Langmuir* **2005**, *21*, 956–961.
- Shibuichi, S.; Onda, T.; Satoh, N.; Tsujii, K. Super Water-Repellent Surfaces Resulting from Fractal Structure. *J. Phys. Chem.* **1996**, *100*, 19512–19517.
- Bico, J.; Tordeux, C.; Quééré, D. Rough Wetting. *Europhys. Lett.* **2001**, *55*, 214–220.
- Quééré, D. Rough Ideas on Wetting. *Phys. A* **2002**, *313*, 32–46.
- Martines, E.; Seunarine, K.; Morgan, H.; Gadegaard, N.; Wilkinson, C. D. W.; Riehle, M. O. Superhydrophobicity and Superhydrophilicity of Regular Nanopatterns. *Nano Lett.* **2005**, *5*, 2097–2103.
- Ou, J.; Perot, B.; Rothstein, J. P. Laminar Drag Reduction in Microchannels Using Ultrahydrophobic Surfaces. *Phys. Fluids* **2004**, *16*, 4635–4643.



17. Joseph, P.; Cottin-Bizonne, C.; Benoit, J. M.; Ybert, C.; Journet, C.; Tabeling, P.; Bocquet, L. Slippage of Water Past Superhydrophobic Carbon Nanotube Forests in Microchannels. *Phys. Rev. Lett.* **2006**, *97*, 156104.
18. Xu, X. M.; Vereecke, G.; Hoogen, E.; van den Smeers, J.; Armini, S.; Delande, T.; Struyf, H. Wetting Challenges in Cleaning of High Aspect Ratio Nano-Structures. *Solid State Phenom.* **2012**, *195*, 235–238.
19. Extrand, C. W.; Moon, S. I.; Hall, P.; Schmidt, D. Superwetting of Structured Surfaces. *Langmuir* **2007**, *23*, 8882–8890.
20. Yuan, J.; Liu, X.; Akbulut, O.; Hu, J.; Suib, S. L.; Kong, J.; Stellacci, F. Superwetting Nanowire Membranes for Selective Absorption. *Nat. Nanotechnol.* **2008**, *3*, 332–336.
21. Barbieri, L.; Wagner, E.; Hoffmann, P. Water Wetting Transition Parameters of Perfluorinated Substrates with Periodically Distributed Flat-Top Microscale Obstacles. *Langmuir* **2007**, *23*, 1723–1734.
22. Neinhuis, C.; Barthlott, W. Characterization and Distribution of Water-Repellent, Self-Cleaning Plant Surfaces. *Ann. Bot.* **1997**, *79*, 667–677.
23. Sun, T. L.; Feng, L.; Gao, X. F.; Jiang, L. Bioinspired Surfaces with Special Wettability. *Acc. Chem. Res.* **2005**, *38*, 644–652.
24. Feng, L.; Zhang, Y. A.; Xi, J. M.; Zhu, Y.; Wang, N.; Xia, F.; Jiang, L. Petal Effect: A Superhydrophobic State with High Adhesive Force. *Langmuir* **2008**, *24*, 4114–4119.
25. Tong, L. M.; Gattass, R. R.; Ashcom, J. B.; He, S. L.; Lou, J. Y.; Shen, M. Y.; Maxwell, I.; Mazur, E. Subwavelength-Diameter Silica Wires for Low-Loss Optical Wave Guiding. *Nature* **2003**, *426*, 816–819.
26. Spori, D. M.; Drobek, T.; Zürcher, S.; Ochsner, M.; Sprecher, C.; Mühlebach, A.; Spencer, N. D. Beyond the Lotus Effect: Roughness Influences on Wetting over a Wide Surface-Energy Range. *Langmuir* **2008**, *24*, 5411–5417.
27. Oner, D.; McCarthy, T. J. Ultrahydrophobic Surfaces. Effects of Topography Length Scales on Wettability. *Langmuir* **2000**, *16*, 7777–7782.
28. Yoshimitsu, Z.; Nakajima, A.; Watanabe, T.; Hashimoto, K. Effects of Surface Structure on the Hydrophobicity and Sliding Behavior of Water Droplets. *Langmuir* **2002**, *18*, 5818–5822.
29. Vrancken, R. J.; Blow, M. L.; Kusumaatmaja, H.; Hermans, K.; Prenen, A. M.; Bastiaansen, C. W. M.; Broer, D. J.; Yeomans, J. M. Anisotropic Wetting and de-Wetting of Drops on Substrates Patterned with Polygonal Posts. *Soft Matter* **2013**, *9*, 674–683.
30. Abdelsalam, M. E.; Bartlett, P. N.; Kelf, T.; Baumberg, J. Wetting of Regularly Structured Gold Surfaces. *Langmuir* **2005**, *21*, 1753–1757.
31. Tuteja, A.; Choi, W.; Ma, M.; Mabry, J. M.; Mazzella, S. a.; Rutledge, G. C.; McKinley, G. H.; Cohen, R. E. Designing Superoleophobic Surfaces. *Science* **2007**, *318*, 1618–1622.
32. Tuteja, A.; Choi, W.; Mabry, J. M.; McKinley, G. H.; Cohen, R. E. Robust Omniphobic Surfaces. *Proc. Natl. Acad. Sci. U. S. A.* **2008**, *105*, 18200–18205.
33. Herminghaus, S. Roughness-Induced Non-Wetting. *Europhys. Lett.* **2000**, *52*, 165–170.
34. Lafuma, A.; Quéré, D. Superhydrophobic States. *Nat. Mater.* **2003**, *2*, 457–460.
35. McHale, G.; Aqil, S.; Shirtcliffe, N. J.; Newton, M. I.; Erbil, H. Y. Analysis of Droplet Evaporation on a Superhydrophobic Surface. *Langmuir* **2005**, *21*, 11053–11060.
36. Reyssat, M.; Yeomans, J. M.; Quéré, D. Impalement of Fakir Drops. *Europhys. Lett.* **2008**, *81*, 26006.
37. Vos, I.; Hellin, D.; Vertommen, J.; Demand, M.; Boullart, W. Silicon Nano-Pillar Test Structures for Quantitative Evaluation of Wafer Drying Induced Pattern Collapse. *ECS Trans.* **2011**, *41*, 189–196.
38. Johnson, R. E.; Dettre, R. H. Contact Angle Hysteresis. *Adv. Chem. Ser.* **1964**, *43*, 112–135.
39. Extrand, C. W. Model for Contact Angles and Hysteresis on Rough and Ultraphobic Surfaces. *Langmuir* **2002**, *1*, 7991–7999.
40. Patankar, N. A. On the Modeling of Hydrophobic Contact Angles on Rough Surfaces. *Langmuir* **2003**, *19*, 1249–1253.
41. McHale, G.; Shirtcliffe, N. J.; Newton, M. I. Contact-Angle Hysteresis on Super-Hydrophobic Surfaces. *Langmuir* **2004**, *20*, 10146–10149.
42. Moulinet, S.; Bartolo, D. Life and Death of a Fakir Droplet: Impalement Transitions on Superhydrophobic Surfaces. *Eur. Phys. J. E* **2007**, *24*, 251–260.
43. Saad, N.; Dufour, R.; Campistron, P.; Nassar, G.; Carlier, J.; Harnois, M.; Merheb, B.; Boukherroub, R.; Senez, V.; Gao, J.; et al. Characterization of the State of a Droplet on a Micro-Textured Silicon Wafer Using Ultrasound. *J. Appl. Phys.* **2012**, *112*, 104908.
44. Seo, K.; Wober, M.; Steinvurzel, P.; Schonbrun, E.; Dan, Y. P.; Ellenbogen, T.; Crozier, K. B. Multicolored Vertical Silicon Nanowires. *Nano Lett.* **2011**, *11*, 1851–1856.
45. Marmur, A. The Lotus Effect: Superhydrophobicity and Metastability. *Langmuir* **2004**, *20*, 3517–3519.
46. Plimpton, S. Fast Parallel Algorithms for Short Range Molecular Dynamics. *J. Comput. Phys.* **1995**, *117*, 1–19. <http://lammps.sandia.gov>.
47. Joly, L. Capillary Filling with Giant Liquid/solid Slip: Dynamics of Water Uptake by Carbon Nanotubes. *J. Chem. Phys.* **2011**, *135*, 214705.
48. Lundgren, M.; Allan, N. L.; Cosgrove, T.; George, N. Molecular Dynamics Study of Wetting of a Pillar Surface. *Langmuir* **2003**, *19*, 7127–7129.
49. Hong, S. D.; Ha, M. Y.; Balachandar, S. Static and Dynamic Contact Angles of Water Droplet on a Solid Surface Using Molecular Dynamics Simulation. *J. Colloid Interface Sci.* **2009**, *339*, 187–195.
50. Shen, P.; Fujii, H.; Nogi, K. Effect of Substrate Crystallographic Orientation on Wettability and Adhesion in Several Representative Systems. *J. Mater. Process. Technol.* **2004**, *155*, 1256–1260.
51. Israelachvili, J. N. *Intermolecular and Surface Forces*; 2nd ed.; Academic Press: San Diego, CA, 1991.